



Sputtered amorphous thin film nanocomposites as an anode for lithium-ion batteries



Si-Jin Kim, Han-Chul Park, Min-Cheol Kim, Da-Mi Kim, Young-Woo Lee, Kyung-Won Park*

Department of Chemical Engineering, Soongsil University, Seoul 156-743, Republic of Korea

HIGHLIGHTS

- Nanocomposites for lithium ion batteries are prepared via a sputtering deposition method.
- The nanocomposites consist of amorphous Ge and TiN phases.
- The Ge–TiN nanocomposites demonstrate relatively high reversible capacities.
- The Ge–TiN nanocomposites show good capacity retention ratios.
- The Ge–TiN nanocomposites show excellent high rate cycling performance.

ARTICLE INFO

Article history:

Received 7 July 2014

Received in revised form

24 September 2014

Accepted 25 September 2014

Available online 2 October 2014

Keywords:

Nanocomposite

Germanium

Titanium nitride

Sputtering

Anode

Lithium-ion batteries

ABSTRACT

In order to overcome the pulverization problem of Ge-based anode materials with high capacity, we use the co-sputtering deposition method to prepare thin film nanocomposites (Ge–TiN), containing amorphous Ge and TiN, as an anode for use in high-performance LIBs. Compilation of the data from XRD, Raman, and TEM suggests that the nanocomposites consist of amorphous Ge and TiN phases in the presence of phase separation. From the XPS and EDX data, the nanocomposites show homogeneous distribution of Ge and TiN both on the surface and in the bulk of the electrodes. In the active–inactive composite, Ge acts as a reactant during the lithiation process, forming Li_xGe , which is surrounded by an inactive TiN matrix. The Ge–TiN nanocomposites demonstrate relatively high reversible capacities, and show good capacity retention ratios and excellent high rate cycling performance even at a high current rate.

© 2014 Elsevier B.V. All rights reserved.

1. Introduction

Lithium-ion batteries (LIBs) are attractive portable electrochemical power sources due to their high cell voltage, high energy density, and excellent cycle life. The traditional graphite anode of LIBs, with a theoretical specific capacity of 372 mAh g^{-1} , exhibits chemical stability, low irreversible capacity loss, and low cost [1–3]. However, group IV materials, such as Si and Ge, have recently attracted a lot of attention for high capacity applications, as they can accommodate as much as 4.4Li^+ per formula unit [4–6], exhibiting high theoretical capacities of $\sim 4130 \text{ mAh g}^{-1}$ (Si) [7,8] and $\sim 1624 \text{ mAh g}^{-1}$ (Ge) [9–11]. Compared to Si-based electrodes, Ge-based materials show more promise due to their higher Li diffusivity for high-power rate anodes, and excellent electrical

conductivity conferred by the smaller band gap of 0.6 V [12,13]. During the insertion/desertion process, Ge undergoes lithium alloying/dealloying reactions: $\text{Ge} + 4.4\text{Li}^+ + 4.4\text{e}^- = \text{Li}_{4.4}\text{Ge}$ [14]. Unfortunately, this process can induce volume changes of up to 400%, resulting in mechanical stress which can cause cracking and pulverization of the Ge electrodes, leading to capacity fading and poor cycle life [2,3,12].

Much effort has been made to minimize such volume strain during charge and discharge [9–11,15–20], in order to preserve the electrical pathways and to improve cyclability [21–25]. Huggins and co-workers first proposed the use of active–inactive composites as a mixed-conductor matrix concept to overcome pulverization of the anode materials, which electrically isolates the active particles from the current collector [26]. The inactive phase can prevent aggregation of the particles and act as an electrically connecting medium between the anode particles and the current collector [11,15,16,27]. Titanium nitride (TiN) is well-known for its excellent chemical resistance, superior electrical conductivity, and

* Corresponding author. Fax: +82 2 812 5378.

E-mail addresses: kwpark@ssu.ac.kr, snow7292@naver.com (K.-W. Park).

good adhesion with most materials [28–30]. Therefore, in this work, thin film nanocomposites containing amorphous Ge and TiN (Ge–TiN) were prepared by the radio frequency (RF) magnetron sputtering method for use as an anode for high-performance LIBs. In the active–inactive composite, consisting of Ge and TiN, the Ge acts as a reactant during the lithiation process to form Li_xGe , which is surrounded by the TiN inactive matrix. The TiN in the composite electrode may not alloy with lithium, serving as an inactive matrix to support the intergrain electronic contact in the material. The Ge–TiN nanocomposite delivered a high reversible capacity, and demonstrated good capacity retention after cycling, and high reversible capacity even at high C rate discharging.

2. Experimental

Ge–TiN nanocomposite electrodes were grown using an RF magnetron co-sputtering system with a dual sputtering-gun. Pure Ge (99.999%, LTS Chemical) and TiN (99.9%, LTS Chemical) were used as the target materials [31,32]. Si (100) and Cu foil were used as substrates to characterize the structural and electrochemical properties, respectively. In order to fabricate optimized Ge–TiN electrodes, the co-sputtering deposition was performed with varying RF powers (Ge = 40 W, TiN = 40, 60, and 80 W) under Ar gas flowed at 30 SCCM at room temperature for 30 min. The base pressure was less than 5×10^{-6} torr, and the working pressure was 1.1×10^{-2} torr. The sputtering process was carried out with continuous rotation to obtain uniform thin films [33]. The average loading amount of active materials for all electrodes was $\sim 75 \mu\text{g cm}^{-2}$.

The morphology of the samples was characterized by FE-TEM and HAADF-STEM using a Tecnai G2 F30 system operating at 300 kV. EDX analysis of the samples was also performed on the Tecnai system using a field emission gun (FEG) analytical electron microscope, equipped with a Gatan image filter and operated at 300 kV. Calculations for quantitative STEM-EDX mapping and line scans were conducted offline using ES Vision v4.0.172. The sample holder was tilted by 30° with respect to the electron beam to optimize the fluorescence detection. Different dwell times were tested in order to find an optimum value (4 s per point) which avoided beam damage while still providing reasonable counting statistics. The spatial resolution was given by the 3 nm diameter of the electron beam. TEM samples were prepared by sputtering the nanocomposites on a carbon-coated copper grid substrate. The thickness of the samples was measured using a field emission scanning electron microscopy (FE-SEM JSM-6700F, Eindhoven, Nederland).

For structure analysis of the electrodes, XRD (D2 PHASER, Bruker AXS) analysis was carried out using a Bruker X-ray diffractometer with a $\text{Cu K}\alpha$ ($\lambda = 0.15418 \text{ nm}$) source and a Ni filter. The source was operated at 30 kV and 10 mA. The 2θ angular scan was performed from 10° to 80° at a scan rate of $0.5^\circ \text{ min}^{-1}$. Raman spectra were recorded on a high resolution Mirco-Raman spectrometer (LabRam Aramis, Horriba Jovin Yvon) using an Ar ion laser with $\lambda = 532.8 \text{ nm}$. XPS (XPS, Thermo VG, U.K.) analysis was carried out with an Al $\text{K}\alpha$ X-ray source of 1486.6 eV at a chamber pressure below 1×10^{-8} Torr and a beam power of 200 W. All high resolution spectra were collected using pass energy of 46.95 eV. The step size and time per step were set at 0.025 eV and 100 ms, respectively. Both ends of the baseline were set sufficiently far apart so as not to distort the shape of the spectra, including the tails. Small variation in the range of the baseline did not affect the relative amount of fitted species (less than 1%). The C 1s electron binding energy was referenced at 284.6 eV, and a nonlinear least-squares curve-fitting program was employed with a Gaussian–Lorentzian production function.

To assemble lithium coin cells for testing (size 2032, Hohsen Corporation), the Ge–TiN nanocomposite electrodes produced were used as the working electrode, and were evaluated with respect to lithium foil (FMC Corporation) as the counter electrode. The electrodes, with an area of 1.32 cm^2 , were dried at 70°C in a vacuum oven. The coin cells were assembled inside an argon-filled glove box ($<5 \text{ ppm}$, H_2O and O_2). The electrodes of the cells were separated by a porous polypropylene membrane (Celgard 2400) and an electrolyte solution consisting of 1.1 M LiPF_6 in (ethylene carbonate:dimethyl carbonate) = (1:1) as a solvent mixture (Soulbrain Co., Ltd.). After assembly into coin cells, charge–discharge cycling was performed on a multichannel battery tester (WBCS300L, Wonatech Co.). The coin cells were cycled between 0.01 and 3.0 V vs. Li/Li^+ at various currents with a rest period for 30 min between charge (galvanostatic and potentiostatic mode)/discharge (galvanostatic mode) at 25°C .

3. Results and discussion

Fig. 1 shows a schematic illustration of the fabrication of the nanocomposite electrodes on a Cu-foil substrate via a co-sputtering deposition system using two sputtering guns of Ge and TiN. The Ge–TiN electrodes (denoted as GT-0, GT-40, GT-60, and GT-80) were deposited with varying RF powers of the TiN target, at 0, 40, 60, and 80 W, and a fixed 40 W for the Ge target [31–34]. Fig. 2(a) shows the XRD patterns of the various nanocomposite electrodes sputtered at room temperature. Peaks for Ge and TiN did not appear, indicating formation of the amorphous phases, except for XRD peaks at 43.15° , 50.25° , and 73.95° which corresponded to (111), (200), and (220) of a face-centered cubic structure of Cu (JCPDS 03-1005) as a current collector. It was reported that the utilization of electrodes with amorphous structure could lead to homogeneous volume expansions, resulting in improved cycling performance [34–38]. The Raman spectra of GT-0, GT-40, GT-60, and GT-80 were obtained using an excitation wavelength of 532.8 nm, as indicated in Fig. 2(b), in which the characteristic peaks of amorphous Ge and TiN were observed. The Raman spectra were dominated by broad bands at 274 and 514 cm^{-1} [15,33], corresponding to the amorphous Ge–Ge and TiN–TiN phonon modes, respectively. A band at 303 cm^{-1} , associated with crystalline Ge, was not detected, nor was the Ge–TiN phonon mode related with alloy formation [10,16]. This demonstrates the phase separation between Ge and TiN in the nanocomposites formed by the co-sputtering deposition method at room temperature. Compiling the data from XRD and Raman, it can

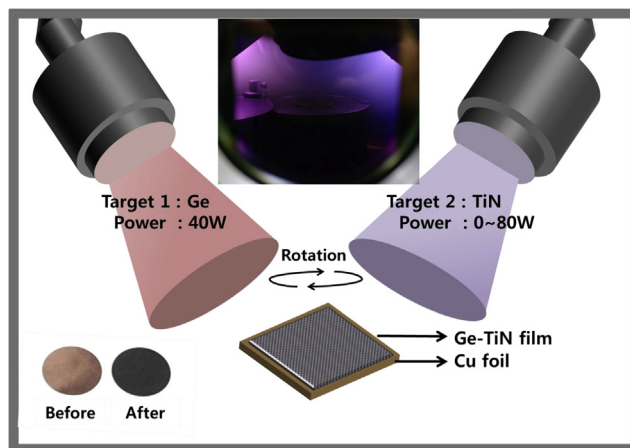


Fig. 1. A schematic illustration of the fabrication of nanocomposites via a co-sputtering deposition system with two sputtering targets of Ge and TiN.

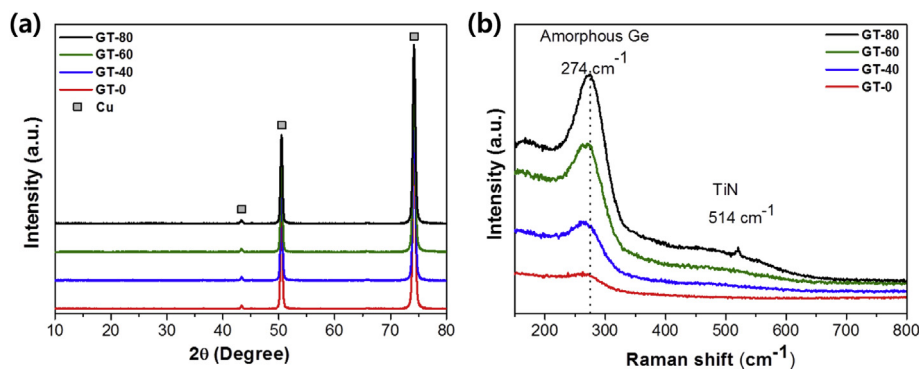


Fig. 2. (a) XRD patterns and (b) Raman spectra of the as-prepared nanocomposites.

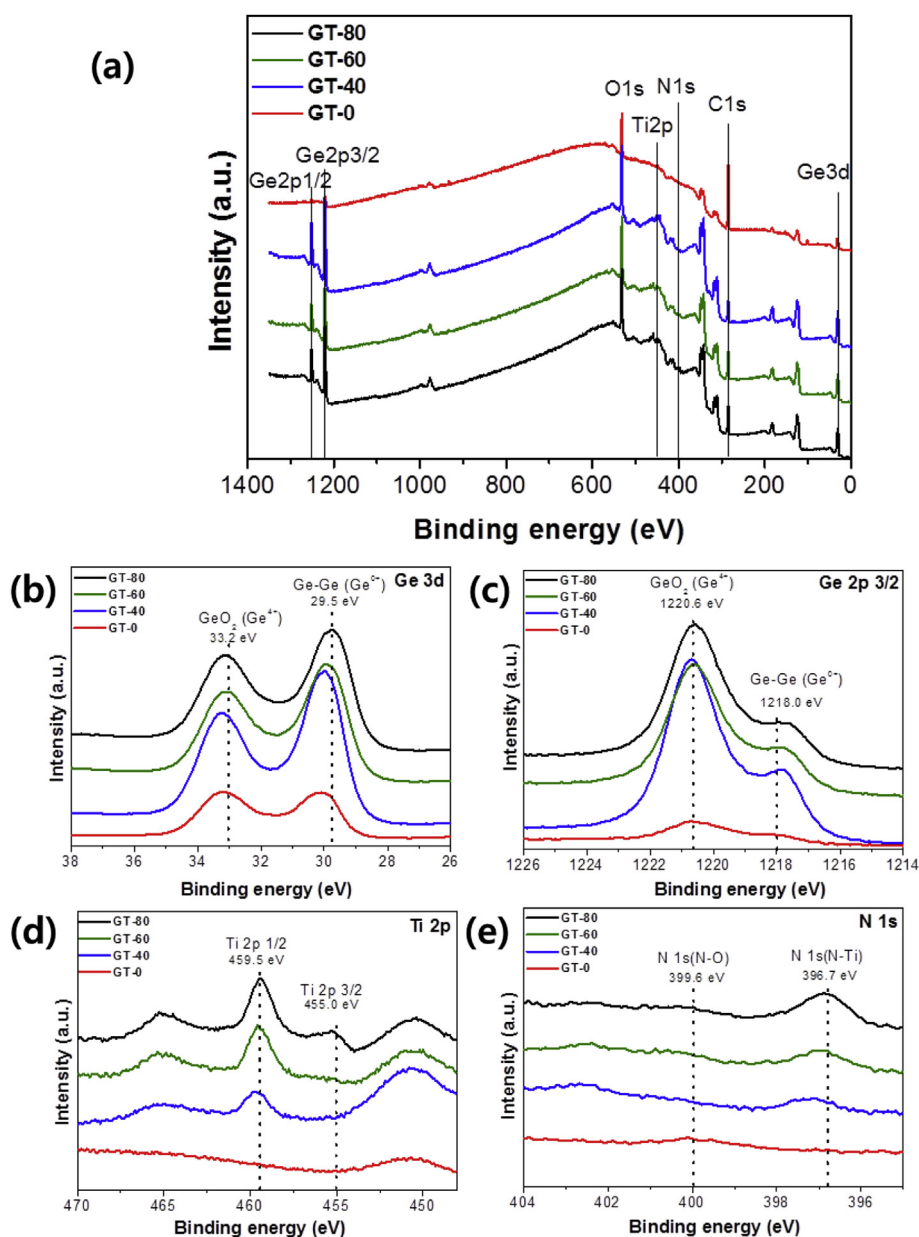


Fig. 3. (a) Wide scan, (b) Ge 3d, (c) Ge 2p, (d) Ti 2p, and (e) N 1s XPS peaks of the as-prepared nanocomposites.

be inferred that the nanocomposites consisted of amorphous Ge and TiN phases in the presence of phase separation.

Fig. 3 shows wide and fine scan XPS spectra of the samples. The Ge 3d peaks for the nanocomposites contained Ge^{4+} at 33.2 eV, as well as Ge^0 at 29.5 eV (Fig. 3(b)). The Ge $2p_{3/2}$ peaks consisted of Ge^{4+} and Ge^0 at 1220.6 eV and 1218.0 eV, respectively (Fig. 3(c)) [39,40]. In particular, the existence of Ge^{4+} might result from natural surface oxidation of Ge in an air atmosphere after the sputtering process. The Ti $2p_{1/2}$ and $2p_{3/2}$ spectra for GT-40, GT-60, and GT-80 appeared at 459.5 and 455.0 eV, respectively. In addition, GT-40, GT-60, and GT-80 exhibited XPS peaks associated with N–O (399.6 eV) and N–Ti (396.7 eV) [20,36]. The XPS spectra revealed the elemental compositions of Ge and TiN in the nanocomposites to be as follows: 96.12 at% Ge and 3.87 at% TiN in GT-40; 90.75 at% Ge and 9.25 at% TiN in GT-60; and 88.48 at% Ge and 11.52 at% TiN in GT-60.

Fig. 4 shows TEM images of the as-prepared GT-0, GT-40, GT-60, and GT-80, made by controlling the power ratio of the sputtering gun for Ge and the TiN target in the RF magnetron sputtering system. In the TEM images, the size of the nanocomposites seemed to increase with an increasing sputtering power ratio of the TiN target. However, the fast Fourier transform (FFT) patterns of the samples confirmed the formation of amorphous Ge phases (insets of Fig. 4(e)–(h)). According to the EDX data (Fig. 5), the elemental compositions of Ge and TiN in the nanocomposites were as follows: 96.06 at% Ge and 3.94 at% TiN in GT-40; 91.80 at% Ge and 8.20 at% TiN in GT-60; and 88.22 at% Ge and 11.78 at% TiN in GT-80. Table 1 displays the relative atomic ratios of Ge and TiN for the samples, as determined by the XPS and EDX data. This demonstrates that with increasing power of the TiN target, from 40 to 80 W, the relative elemental compositions of TiN in the nanocomposite samples also increased. By comparing the XPS and EDX data, it can be concluded that the nanocomposites showed homogeneous distribution of Ge and TiN on the surface and in the bulk of the electrodes. Fig. 6 shows TEM images and the line profiles of the as-prepared GT-0, GT-40, GT-60, and GT-80. The elemental line profiles were acquired along the sample spectrum images of the overall structure. With increasing power of the TiN target, the relative count numbers of the TiN phase increased, demonstrating increased chemical

composition of the TiN phase in the samples (Fig. 6(e)–(h)). The interesting configuration of the Ge–TiN nanostructure electrodes is the phase separation between metallic Ge and TiN without a solid solution. It has been reported that Ge has a higher surface energy ($1060\text{--}1300\text{ mJ m}^{-2}$) than TiN (63.2 mJ m^{-2}) [41,42]. Since the surface energy can determine whether one material wets another, it can be expected that during the deposition process in the sputtering system, the high-surface-energy Ge may tend to form nanophases surrounded by the low-surface-energy TiN. In other words, it is inferred that nanosized Ge is spontaneously formed with TiN due to the differences of surface energy between the two. Accordingly, the as-deposited electrodes exhibited a nanocomposite structure consisting of Ge and TiN. In the nanocomposites, the Ge nanophases were surrounded by the TiN, forming a clear interface between the two. The anode layers of the GT-0, GT-40, GT-60, and GT-80 thin films were 180.9, 170.6, 163.1, and 152.8 nm thick, respectively (The cross-sectional FE-SEM images of Fig. 7). With increasing power of the TiN target, the thickness of the as-prepared electrodes decreased. In the sputtering process of one component, the thickness of the sputtered electrode general increases due to the shadowing effect with increasing power in the sputtering system. However, Karabacak and co-workers reported that in the co-sputtering system with two components having different surface energies, the thickness of the sputtered electrodes might not increase with increasing sputtering power due to a competition between shadowing effect of high-surface-energy material (Ge) and re-emission of low-surface-energy material (TiN) [43].

Fig. 8 shows the voltage profiles of the as-prepared anodes in the 1st and 2nd cycles between 3.0 and 0 V at a current density of 1 A g^{-1} in coin-type half-cells. The 1st discharge capacities of the GT-0, GT-40, GT-60, and GT-80 electrodes were 1536.67, 1445.96, 1242.01, and 1154.82 mAh g^{-1} , respectively. The capacity retention ratios (100th/2nd cycle) the GT-0, GT-40, GT-60, and GT-80 electrodes were 40.02%, 58.05%, 43.61%, and 42.88%, respectively. All the nanocomposites exhibited relatively low 1st capacities and high capacity retention ratios compared to GT-0. All the nanocomposites exhibited low 1st capacities and high capacity retentions compared to GT-0. However, as the amount of TiN in the nanocomposite

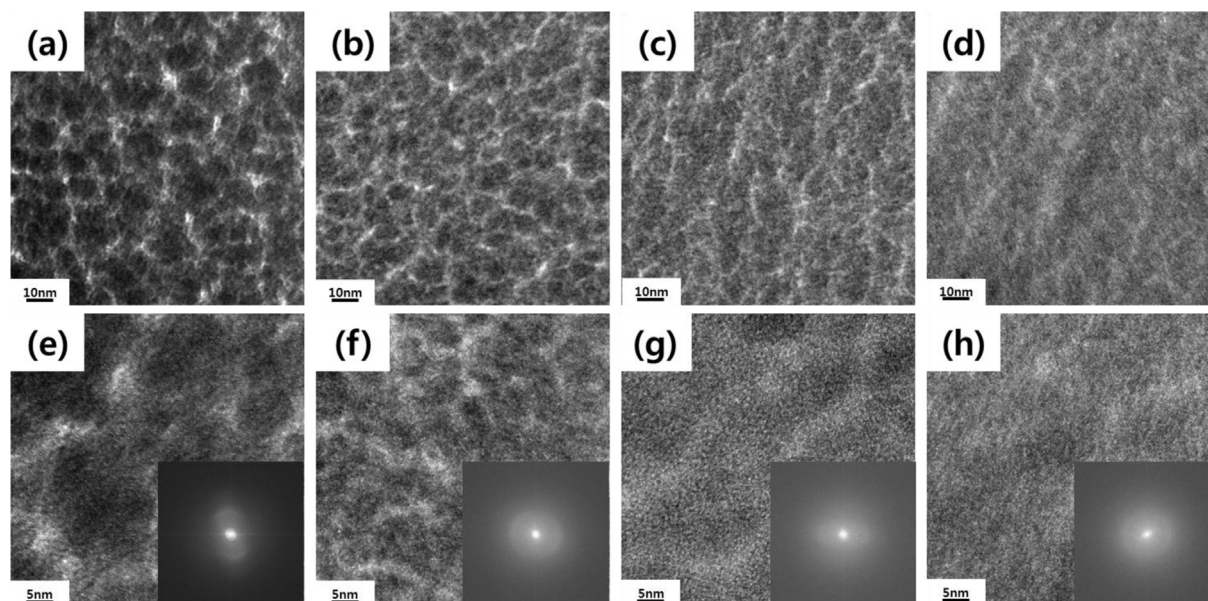


Fig. 4. FE-TEM and high-resolution images, respectively, of the as-prepared GT-0 (a, e), GT-40 (b, f), GT-60 (c, g), and GT-80 (d, h). The insets indicate the FFT patterns of the samples.

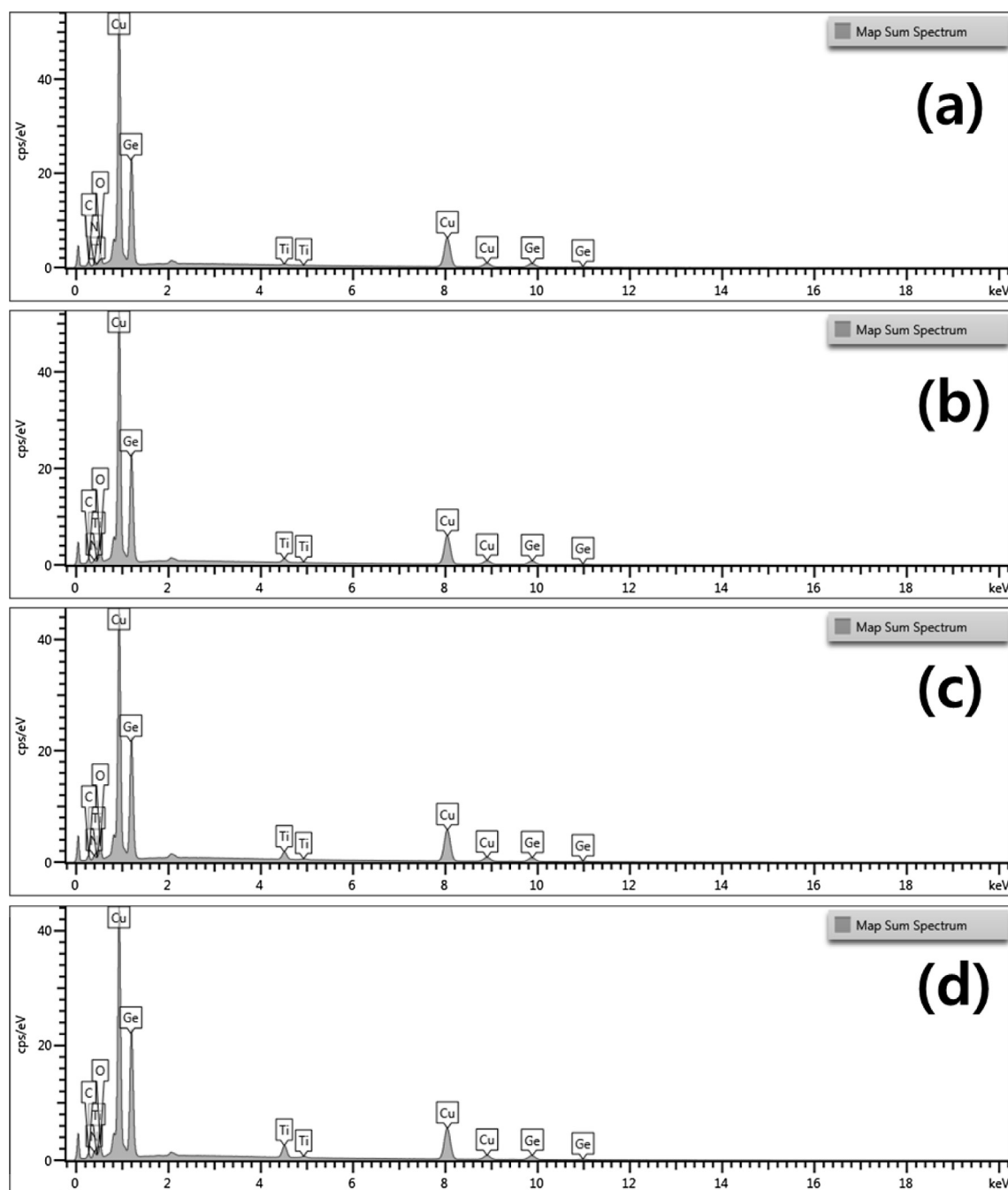


Fig. 5. EDX spectra of the as-prepared GT-0 (a), GT-40 (b), GT-60 (c), and GT-80 (d).

anodes increased, the reversible discharge capacity steadily decreased. It has been reported that the use of TiN as an anode material exhibits a reversible discharge capacity of 120 mAh g^{-1} [28,29]. However, the sputtered TiN in the GT-40, GT-60, and GT-80

Table 1
Relative atomic ratio of Ge and TiN for the as-prepared samples determined by the XPS and EDX analysis.

Samples	XPS		EDX	
	Ge (at%)	TiN (at%)	Ge (at%)	TiN (at%)
GT-0	100	0	100	0
GT-40	96.12	3.87	96.06	3.94
GT-60	90.75	9.25	91.80	8.20
GT-80	88.48	11.51	88.22	11.78

nanocomposites can be considered as an inactive matrix due to the relatively small portion in the electrodes and the high current rate operation.

In order to confirm the voltage range for the lithiation reaction in the anodes, the differential discharge capacity plots were obtained at a current density of 1 A g^{-1} for the as-prepared anodes containing different amounts of TiN, as shown in Fig. 9. The differential analysis curves were measured between 3.0 and 0 V by simultaneously obtaining voltage profiles of Figs. 8 and 10. However, the characteristic reduction peaks related to Li and Ge appeared between 1.1 and 0.01 in the differential discharge capacity curves. The voltage plot of the lithiation process between Li and Ge exhibited multiple peaks for GT-0, corresponding to $\text{Li}_{22}\text{Ge}_5$ and $\text{Li}_{15}\text{Ge}_4$ at 0.1–0.3 V and Li_7Ge_2 at 0.3–0.5 V, which are

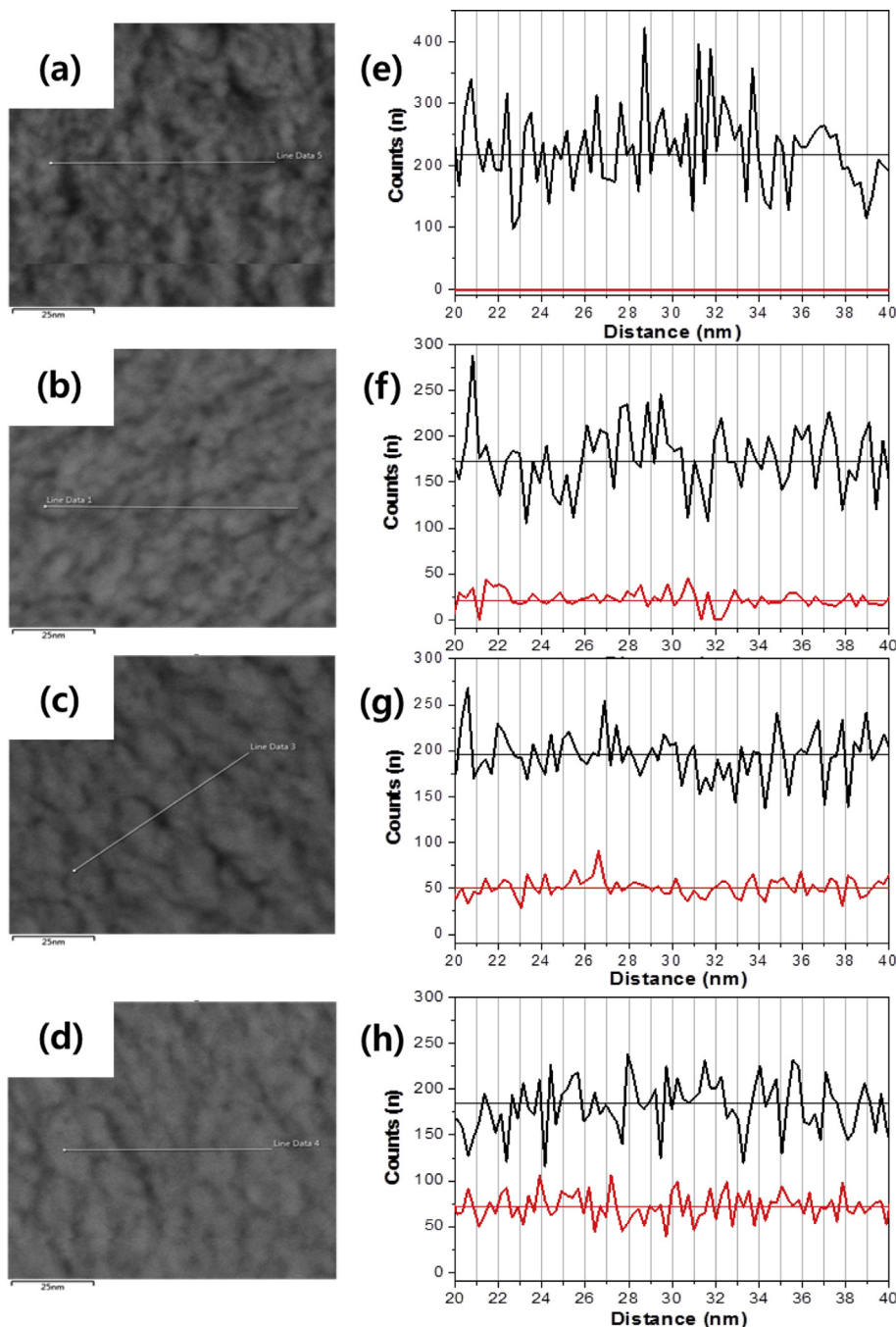


Fig. 6. TEM images and line profiles, respectively, of the as-prepared GT-0 (a, e), GT-40 (b, f), GT-60 (c, g), and GT-80 (d, h).

consistent with the reported values [23,31,44]. GT-40 also displayed differential discharge peaks identical to those of GT-0. On the other hand, in the case of GT-60 and GT-80, the peaks at 0.1–0.3 and 0.3–0.5 V became broader after 20 cycles, indicating suppression of lithiation process. This implies that including over a certain amount of TiN in the nanocomposite anodes could prevent the lithiation of Ge, thus leading to decreased discharge capacity.

The cycling performance of the nanocomposite anodes for 100 cycles at a current rate of 1 A g^{-1} was presented in Fig. 10. The discharge specific capacities of GT-0, GT-40, GT-60, and GT-80 after 100 cycles were 599.68, 757.85, 491.04, and 449.73 mAh g^{-1} , respectively (Fig. 10(a)). Furthermore, the coulombic efficiencies of GT-0, GT-40, GT-60, and GT-80 after 100 cycles were 97.5, 98.7, 98.5,

and 98.4%, respectively (Fig. S1). Their capacity retentions were 40.02, 58.05, 43.61, and 42.88%, respectively. Plots of the volumetric capacity vs. cycle number were presented in Fig. 10(b). GT-0 exhibited relatively rapid capacity fading, due to pulverization of the anode as a result of the volume change during lithiation/delithiation. It is notable that GT-40 showed considerable improvement in terms of both cyclability and specific capacity retention. To further evaluate and compare the high rate performance of the anodes, the discharge current rate was increased stepwise from 1 to 20 A g^{-1} , as shown in Fig. 11(a). With increasing discharge rate, the specific discharge capacities and efficiencies of the TiN-containing nanocomposite anodes were higher than GT-0 over the entire discharge range (Fig. S2). Especially, on the basis

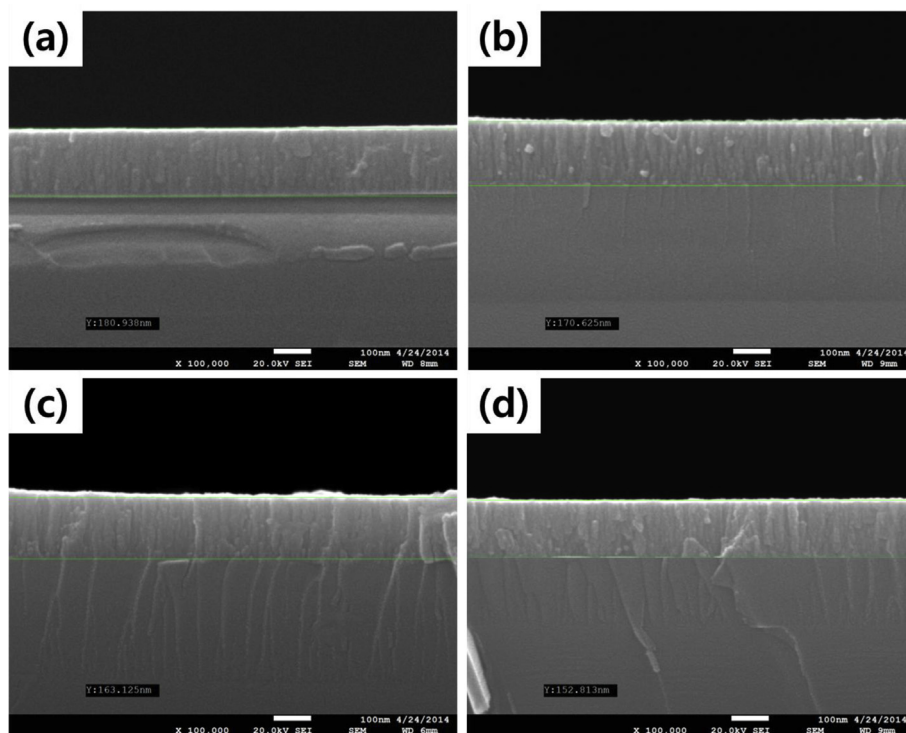


Fig. 7. Cross-sectional SEM images of the as-prepared GT-0 (a), GT-40 (b), GT-60 (c), and GT-80 (d).

of the discharge capacities at 1 A g^{-1} , the nanocomposite anodes showed improved relative retention of the discharge capacity, indicating an excellent high rate cycling performance (Fig. 11(b)).

4. Conclusions

We prepared amorphous Ge and TiN-containing thin film nanocomposites by a co-sputtering method for use as an anode in

high-performance LIBs. The nanocomposites consisted of amorphous Ge and TiN phases with phase separation, and showed homogeneous distribution of Ge and TiN both on the surface and in the bulk of the electrodes. The Ge–TiN nanocomposites exhibited high reversible capacity, good capacity retention, and excellent high rate cycling performance. The improved performance of GT-40, having an optimized amount of TiN as an inactive matrix in the LIBs, may be due to the facilitation of Ge lithiation and the

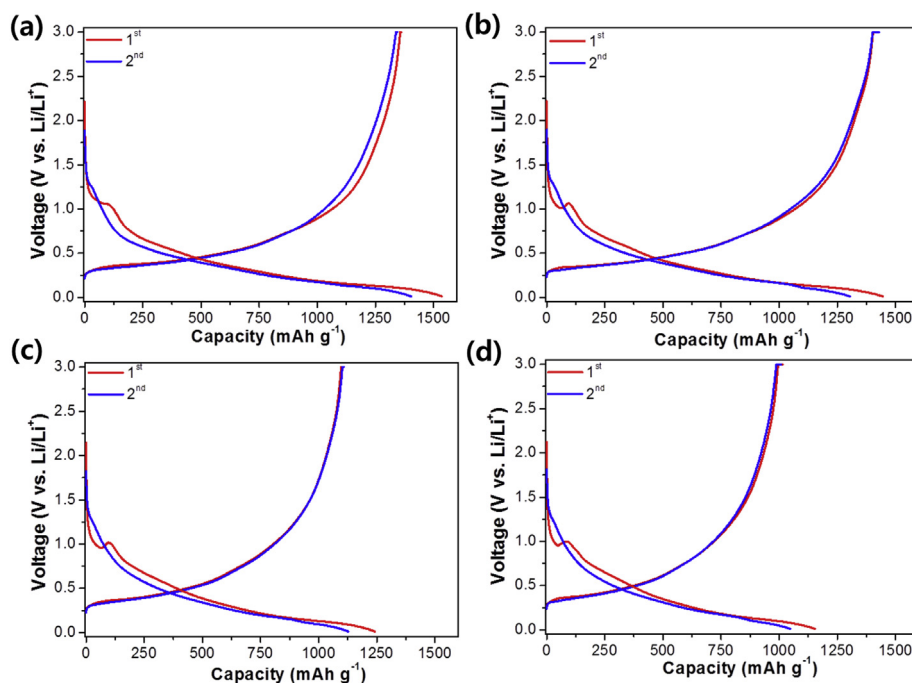


Fig. 8. Voltage profiles of GT-0 (a), GT-40 (b), GT-60 (c), and GT-80 (d) in coin-type half-cells for the 1st, 2nd, 5th, 10th, and 20th cycles between 3.0 and 0 V, at a current density of 1 A g^{-1} .

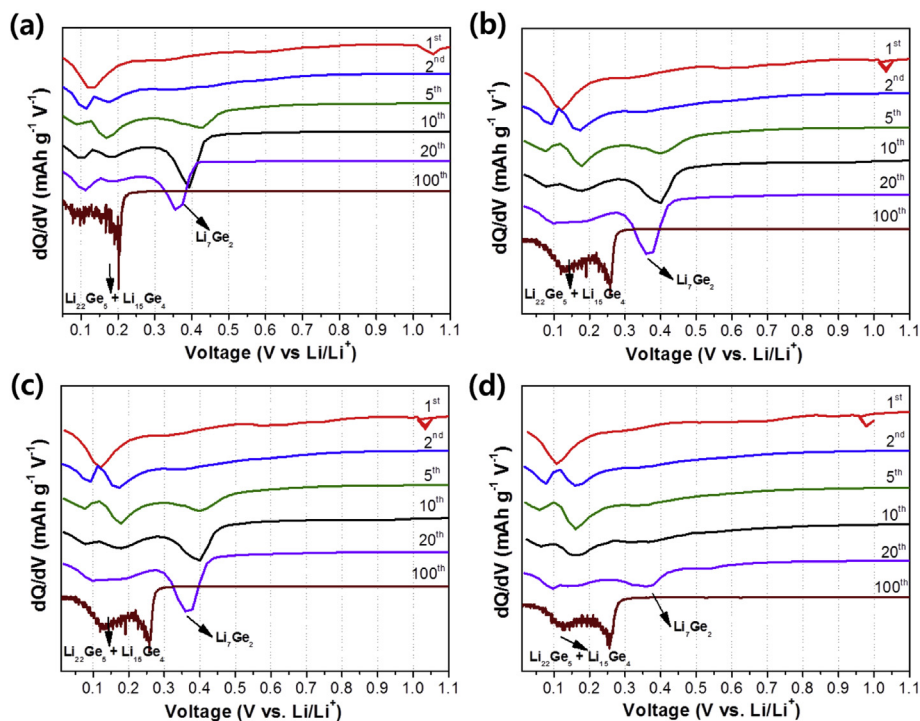


Fig. 9. Differential discharge capacity plots of GT-0 (a), GT-40 (b), GT-60 (c), and GT-80 (d), containing different amounts of TiN, at a current density of 1 A g^{-1} .

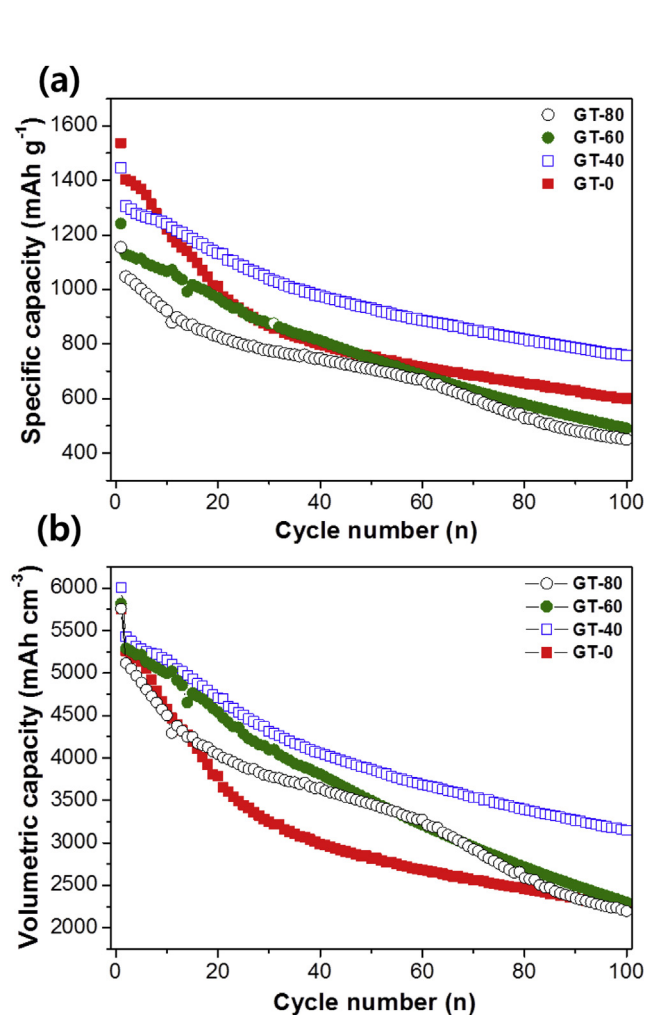


Fig. 10. (a) Specific capacity and (b) volumetric capacity versus cycle number of the nanocomposite anodes for 100 cycles at a current rate of 1 A g^{-1} .

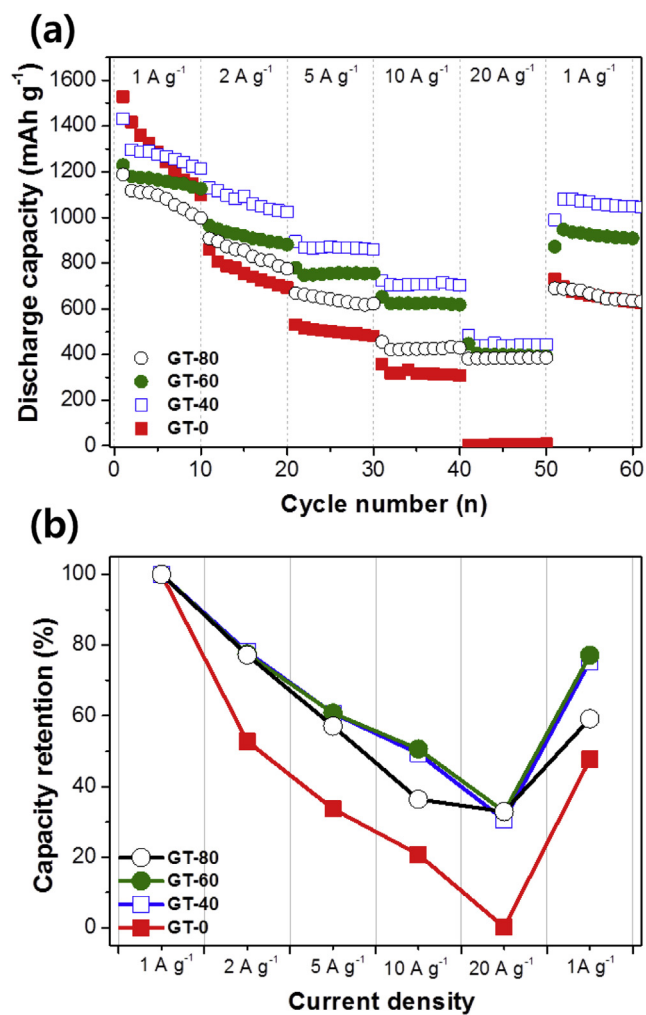


Fig. 11. (a) High rate cycling performance and (b) capacity retention ratio of the nanocomposite anodes from 1 to 20 A g^{-1} .

prevention of pulverization, which can occur as a result of volume changes during lithiation/delithiation.

Acknowledgments

This research was supported by Basic Science Research Program through the National Research Foundation of Korea (NRF) funded by the Ministry of Education (NRF-2013R1A1A2012541).

Appendix A. Supplementary data

Supplementary data related to this article can be found at <http://dx.doi.org/10.1016/j.jpowsour.2014.09.162>.

References

- [1] A.S. Arico, P. Bruce, B. Scrosati, J.-M. Tarascon, W. van Schalkwijk, *Nat. Mater.* 4 (2005) 366–377.
- [2] M. Winter, J.O. Besenhard, M.E. Spahr, P. Novak, *Adv. Mater.* 10 (1998) 725–763.
- [3] M. Winter, J.O. Besenhard, *Electrochim. Acta* 45 (1999) 31–50.
- [4] H. Li, H. Bai, Z. Tao, J. Chen, *J. Power Sources* 217 (2012) 102–107.
- [5] J.-Y. Choi, D. Lee, Y. Lee, Y.-G. Lee, K.M. Kim, J.-K. Park, K.Y. Cho, *Adv. Funct. Mater.* 23 (2013) 2108–2114.
- [6] H. Kim, C.-Y. Chou, J.G. Ekerdt, G.S. Hwang, *J. Phys. Chem. C* 115 (2011) 2514–2521.
- [7] T. Takamura, S. Ohara, M. Uehara, J. Suzuki, K. Sekine, *J. Power Sources* 129 (2004) 96–100.
- [8] A. Magasinski, P. Dixon, B. Hertzberg, A. Kvit, J. Ayala, G. Yushin, *Nat. Mater.* 9 (2010) 353–358.
- [9] D. Li, K.H. Seng, D. Shi, Z. Chen, H.K. Liua, Z. Guo, *J. Mater. Chem. A* 1 (2013) 14115–14121.
- [10] G. Cui, L. Gu, L. Zhi, N. Kaskhedikar, P.A. van Aken, K. Müllen, J. Maier, *Adv. Mater.* 20 (2008) 3079–3083.
- [11] C.K. Chan, X.F. Zhang, Y. Cui, *Nano Lett.* 8 (2007) 307–309.
- [12] A.M. Chockla, M.G. Panthani, V.C. Holmberg, C.M. Hessel, D.K. Reid, T.D. Bogart, J.T. Harris, C.B. Mullins, B.A. Korgel, *J. Phys. Chem. C* 116 (2012) 11917–11923.
- [13] C.S. Fuller, J.C. Severiens, *Phys. Rev.* 96 (1954) 21–24.
- [14] X.H. Liu, S. Huang, S.T. Picraux, J. Li, T. Zhu, J.Y. Huang, *Nano Lett.* 11 (2011) 3991–3997.
- [15] C. Yan, W. Xi, W. Si, J. Deng, O.G. Schmidt, *Adv. Mater.* 25 (2013) 539–544.
- [16] D.-J. Xue, S. Xin, Y. Yan, K.-C. Jiang, Y.-X. Yin, Y.-G. Guo, L.-J. Wan, *J. Am. Chem. Soc.* 134 (2012) 2512–2515.
- [17] D. Wang, Y.-L. Chang, Q. Wang, J. Cao, D.B. Farmer, R.G. Gordon, H. Dai, *J. Am. Chem. Soc.* 126 (2004) 11602–11611.
- [18] S. Fan, L.Y. Lim, Y.Y. Tay, S.S. Pramana, X. Rui, M.K. Samani, Q. Yan, B.K. Tay, M.F. Toney, H.H. Hng, *J. Mater. Chem. A* 1 (2013) 14577–14585.
- [19] H. Lee, J. Cho, *Nano Lett.* 7 (2007) 2638–2641.
- [20] F.-W. Yuan, H.-J. Yang, H.-Y. Tuan, *ACS Nano* 6 (2012) 9932–9942.
- [21] K.H. Seng, M.-H. Park, Z.P. Guo, H.K. Liu, J. Cho, *Angew. Chem. Int. Ed.* 51 (2012) 5657–5661.
- [22] Y. Yu, C. Yan, L. Gu, X. Lang, K. Tang, L. Zhang, Y. Hou, Z. Wang, M.W. Chen, O.G. Schmidt, J. Maier, *Adv. Energy Mater.* 3 (2013) 281–285.
- [23] J. Graetz, C.C. Ahn, R. Yazami, B. Fultz, *J. Electrochem. Soc.* 151 (2004) A698–A702.
- [24] D.T. Ngo, R.S. Kalubarme, M.G. Chourashiya, C.-N. Park, C.-J. Park, *Electrochim. Acta* 116 (2014) 203–209.
- [25] D. Lv, M.L. Gordin, R. Yi, T. Xu, J. Song, Y.-B. Jiang, D. Choi, D. Wang, *Adv. Funct. Mater.* 24 (2013) 1059–1066.
- [26] B.A. Boukamp, G.C. Lesh, R.A. Huggins, *J. Electrochem. Soc.* 128 (1981) 725–728.
- [27] E. Yoo, J. Kim, E. Hosono, H.-S. Zhou, T. Kudo, I. Honma, *Nano Lett.* 8 (2008) 2277–2282.
- [28] D. Lei, T. Yang, B. Qu, J. Ma, Q. Li, L. Chen, T. Wang, *Sustain. Energy* 2 (2014) 1–4.
- [29] Y. Yue, P. Han, X. He, K. Zhang, Z. Liu, C. Zhang, S. Dong, L. Gu, G. Cui, *J. Mater. Chem.* 22 (2012) 4938–4943.
- [30] D. Tang, R. Yi, M.L. Gordin, M. Melnyk, F. Dai, S. Chen, *J. Mater. Chem. A* 2 (2014) 10375–10378.
- [31] B. Laforge, L.L. Jodin, R. Salot, A. Billard, *J. Electrochem. Soc.* 155 (2008) A181–A188.
- [32] M.Q. Snyder, S.A. Trebukhova, B. Ravdel, M.C. Wheeler, J. Dicarilo, C.P. Tripp, W.J. DeSisto, *J. Power Sources* 165 (2007) 379–385.
- [33] Y.H. Cheng, B.K. Tay, S.P. Lau, H. Kupfer, F. Richter, *J. Appl. Phys.* 92 (2002) 1845–1849.
- [34] T. Maruyama, H. Akagi, *J. Electrochem. Soc.* 145 (1998) 1303–1305.
- [35] G.G. Pethuraja, R.E. Welsch, A.K. Sood, C.W. Lee, N.J. Alexander, H. Efstathiadis, P. Haldar, J.L. Harvey, *Mater. Sci. Appl.* 3 (2012) 67–71.
- [36] J. Zheng, J. Hao, X. Liu, W. Liu, *J. Phys. D Appl. Phys.* 45 (2012) 095303/1–095303/9.
- [37] L.Y. Beaulieu, K.W. Eberman, R.L. Turner, L.J. Krause, J.R. Dahn, *Electrochem. Solid-State Lett.* 4 (2001) A137–A140.
- [38] M.G. Kim, J. Cho, *J. Electrochem. Soc.* 156 (2009) A277–A282.
- [39] K. Prabhakaran, T. Ogino, *Surf. Sci.* 325 (1995) 263–271.
- [40] F.-H. Lu, H.-Y. Chen, *Thin Solid Films* 355–356 (1999) 374–379.
- [41] C.-C. Sun, S.-C. Lee, W.-C. Hwang, J.-S. Hwang, I.-T. Tang, Y.-S. Fu, *Mater. Trans.* 47 (2006) 2533–2539.
- [42] R.J. Jaccodine, *J. Electrochem. Soc.* 110 (1963) 524–527.
- [43] T. Karabacak, H. Guclu, M. Yuksel, *Phys. Rev. B* 79 (2009) 195418/1–195418/9.
- [44] S. Yoon, C.-M. Park, H.-J. Sohn, *Electrochem. Solid-State Lett.* 11 (2008) A42–A45.